


Anomalous heavy doping in chemical-vapor-deposited titanium trisulfide nanostructures

Mengxing Sun,^{1,2} Jingzhen Li,³ Qingqing Ji,^{1,*} Yuxuan Lin,¹ Jiangtao Wang,¹ Cong Su,⁴ Ming-Hui Chiu,¹ Yilin Sun^{1,2},, Huayan Si,¹ Tomás Palacios,¹ Jing Lu,⁵ Dan Xie,^{2,†} and Jing Kong^{1,‡}¹Department of Electrical Engineering and Computer Science, Massachusetts Institute of Technology, Cambridge, Massachusetts 02139, USA²Institute of Microelectronics & Beijing National Research Center for Information Science and Technology (BNRist), Tsinghua University, Beijing 100084, China³Key Laboratory of Optoelectronics Technology, College of Microelectronics, Beijing University of Technology, Beijing 100124, China⁴Department of Nuclear Science and Engineering, Massachusetts Institute of Technology, Cambridge, Massachusetts 02139, USA⁵State Key Laboratory for Mesoscopic Physics and Department of Physics, Peking University, Beijing 100871, China

(Received 9 March 2021; accepted 30 August 2021; published 29 September 2021)

Nanoscale transition-metal trichalcogenides such as TiS_3 have shown great potential for both fundamental studies and application developments, yet their bottom-up synthesis strategy is to be realized. Here we explored the chemical vapor deposition (CVD) synthesis of TiS_3 , whose lattice anisotropy has enabled the preferential growth along the b axis, resulting in rectangular nanosheets or nanoribbons with aspect ratios tunable by the growth temperature. The obtained nanostructures, while maintaining the spectroscopic and structural characteristics as that of pristine semiconducting TiS_3 , exhibit high conductivities and ultralow carrier activation barriers, promising as nanoscale conductors. Our experimental and calculation results suggest that the existence of S_2^{2-} vacancies in the CVD-grown TiS_3 is responsible for the heavy n -type doping up to a degenerate level. Moreover, the semiconducting property is predicted to be recovered by passivating the S_2^{2-} vacancies with oxygen atoms from ambient. This work hence portends the tantalizing possibility of constructing nanoscale electronics with defect-engineered trichalcogenide semiconductors.

DOI: [10.1103/PhysRevMaterials.5.094002](https://doi.org/10.1103/PhysRevMaterials.5.094002)

I. INTRODUCTION

Transition-metal trichalcogenides (TMTCs) are a class of layered materials with the general formula of MX_3 , where M is a group-IVB (Ti, Zr, and Hf) or group-VB transition metal (Nb and Ta) and X is a chalcogen (S, Se, and Te) [1,2]. These materials can be regarded as coupled stacks of one-dimensional (1D) molecular wires consisting of face-sharing MX_6 trigonal prisms [2], as shown in Fig. 1(a). For metallic TMTCs, the high electrical conductivity was found to survive in molecular bundles [3–5], making them suitable for nanoscale interconnects in next-generation electronics. However, being metallic in the nanoscale also contributes to the chemical instability in ambient conditions, for which careful surface protection such as h -BN encapsulation has to be implemented to make the 1D TMTCs practically useful [3,5]. Titanium trisulfide (TiS_3), being the focus of this work, belongs to another category among the TMTCs family: rather than a metal, it is an n -type semiconductor with a dimension-insensitive band gap of ~ 1 eV [2,6]. Being structurally and electronically anisotropic [6], this material could be exploited for polarization-sensitive photodetection [7] that holds promise in coherent optical communication. At the same time, when electrically turned on through field-effect

gating, TiS_3 nanoribbons could exhibit high current-carrying capacity that exceeds copper [8]. In this regard, a heavy doping strategy for TiS_3 nanostructures, if possible, could enable new possibilities for nanoscale electronics.

Conventionally, bulk TiS_3 is prepared by time-consuming chemical vapor transport (CVT) techniques that typically last tens of hours [9]. To get thinner two-dimensional layers, mechanical exfoliation method has been used [10,11]; however, they are limited in controllability over thickness and lateral dimensions. On the other hand, bottom-up synthetic strategies such as chemical vapor deposition (CVD) have been recognized as an effective way to grow high-quality nanomaterials such as graphene [12], MoS_2 [13], and TiS_2 [14]. Considering the phase complexity of the Ti-S system [15], as well as the high melting points of both Ti and TiO_2 , it remains an open question until now whether such synthesis method can be extrapolated to grow TiS_3 nanostructures.

We report here heavily doped TiS_3 nanostructures grown by CVD. The TiS_3 nanoribbons and rectangular nanosheets were synthesized on mica substrates, with tunable thickness ranging from several to tens of nanometers. The aspect ratio of the TiS_3 nanostructures could be readily engineered by the growth temperature. Interestingly, our synthesized TiS_3 shows abnormal high conductivity deviating from that of a semiconductor. This nanoscale conductor was further explored by electrical measurements to evaluate its possibility for interconnection. The anomalous conductivity was explained through x-ray photoelectron spectroscopy (XPS) characterization and density-functional theory (DFT)

*qji@mit.edu

†xiedan@tsinghua.edu.cn

‡jingkong@mit.edu

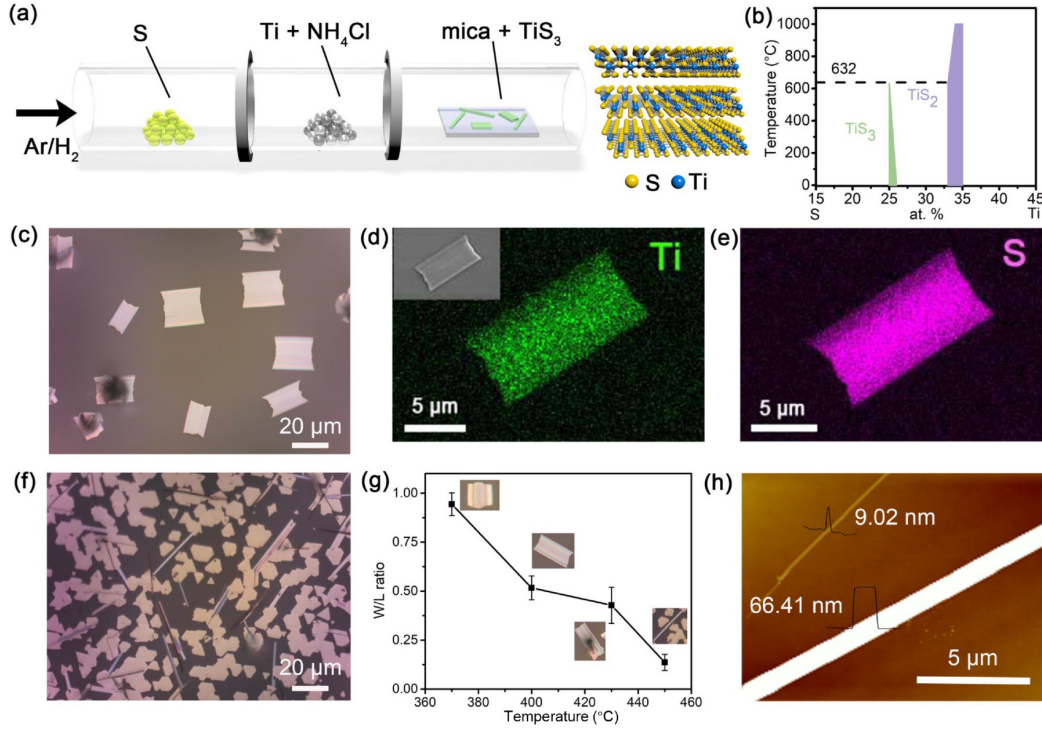
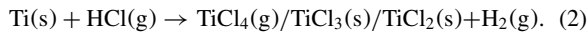
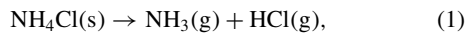


FIG. 1. Atmospheric-pressure CVD (APCVD) growth of TiS_3 . (a) Experimental setup of the APCVD system. The crystal structure of TiS_3 is displayed on the right. (b) Ti-S phase diagram [15]. (c) Typical OM image of TiS_3 nanosheets grown at 400 °C. (d), (e) EDS mapping images of Ti and S, respectively, for a rectangular TiS_3 nanosheet. (f) OM image of mixed TiS_3 nanoribbons and TiS_2 nanosheets grown at 450 °C. (g) Plot of average width/length (W/L) ratio of TiS_3 samples vs the growth temperature. (h) AFM image and height profile of TiS_3 nanoribbons.

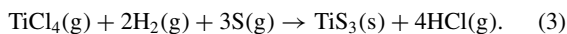
calculation that highlight the important role of S_2^{2-} vacancies. This work demonstrates that trichalcogenide semiconductors are highly susceptible to degenerate doping through defect engineering, which renders them as potential candidates for stable nanoscale interconnection, in addition to their semiconductor functionalities.

II. RESULTS AND DISCUSSION

Figure 1(a) schematically illustrates the TiS_3 CVD synthesis setup in a three-temperature-zone furnace. Considering the high melting point of Ti, NH_4Cl was added to react with Ti to generate the volatile TiCl_4 species:



Under a mixture of Ar/H_2 gas flow, the sulfur and TiCl_4 vapors are conveyed downstream and react into TiS_3 nanostructures on mica:



More details of the sample synthesis are described in Sec. III. It is noteworthy that the reaction of sulfur and the *in situ* generated TiCl_4 can also lead to TiS_2 on mica in a similar condition [14]. According to the Ti-S phase diagram in Fig. 1(b), TiS_3 should be preferentially formed under lower

growth temperature and lower Ti/S atomic ratio in the reacting vapor. This has been experimentally verified by tuning the heating temperature of the sulfur powder and the mica substrate, as will be detailed below.

Figure 1(c) shows the optical microscope (OM) image of the nanosheets synthesized at 400 °C; their thicknesses measured by atomic force microscopy (AFM) are tens of nanometers (Fig. S1 in Supplemental Material (SM) [16]). The well-defined rectangular shape indicates the crystal symmetry in accordance with TiS_3 . Figures 1(d) and 1(e) are the energy-dispersive spectroscopy (EDS) mapping images that clearly exhibit Ti and S distribution over the entire flake area. We found that both insufficient S supply and high growth temperature (e.g., 450 °C) can lead to the formation of a portion of TiS_2 triangles (or truncated triangles) mixed with the TiS_3 nanostructures [Fig. S2 in the SM and Fig. 1(f)], whereas the selective growth of TiS_3 was more robust when the growth temperature decreased to 400 °C or below. Interestingly, the aspect ratio of the TiS_3 nanostructures evolving from nanosheets to nanoribbons is highly dependent on the growth temperature [Fig. 1(g)], which agrees well with the morphological evolution of CVD-synthesized $\text{TiS}_2/\text{TiS}_3$ crystals [17], and demonstrates the potential for in-plane dimension tunability of our CVD method. Figure 1(h) shows the AFM height image of TiS_3 nanoribbons transferred on SiO_2/Si substrate (details of the transfer process can be found in Fig. S3 of the SM); the thicknesses of these nanoribbons were measured to be 10–50 nm. Note that narrower ribbons

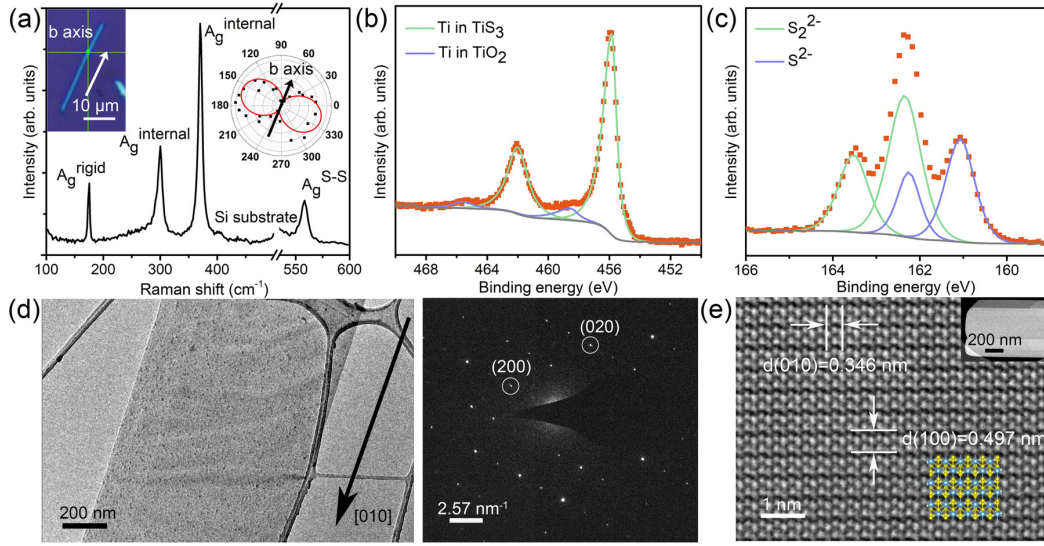


FIG. 2. Characterization of the CVD-synthesized TiS_3 nanostructures. (a) Raman spectrum of TiS_3 . The left inset shows the OM image of the TiS_3 nanoribbon being characterized. The right inset shows the intensity of the A_g^{internal} peak at 371.62 cm^{-1} as a function of the excitation polarization angle. Black dots and red lines are the experimental data of TiS_3 and the $\sin^2\theta$ function-fitted curve, respectively. (b), (c) XPS spectra of Ti and S, respectively, in the TiS_3 samples. (d) TEM image (left) and selected-area electron diffraction patterns (right) of TiS_3 . (e) HAADF-STEM image of TiS_3 . The inset shows the corresponding low-magnification STEM image.

generally have smaller thicknesses, suggesting the possibility of obtaining different thicknesses through seeded growth that limits the ribbon widths. While further efforts are needed to elaborately control the lateral dimension and thickness, the morphological tunability reported here could already enable TiS_3 to be useful in devices of varied dimensions.

We then performed detailed characterizations to examine the composition and lattice structures of the TiS_3 nanoribbons. In the Raman spectrum shown in Fig. 2(a), four distinct peaks at 175.4 cm^{-1} (A_g^{rigid}), 300.1 cm^{-1} (A_g^{internal}), 371.6 cm^{-1} (A_g^{internal}), and 558.3 cm^{-1} ($A_g^{\text{S-S}}$) were identified, which are in good agreement with that of TiS_3 crystals [10]. Further polarized Raman analysis [inset of Fig. 2(a)] was exploited to determine the crystal orientation of the TiS_3 nanoribbons. The A_g^{internal} peak at 371.6 cm^{-1} was found to be weakest when the polarization of excitation was parallel to the nanoribbon, indicating the b axis of TiS_3 along that direction [18]. In the same way, we also spectroscopically identified that the straight edges of the rectangular TiS_3 nanosheets were along the b axis (Fig. S4 of the SM). The peaks at 175.4 cm^{-1} , 300.1 cm^{-1} , and 558.3 cm^{-1} show polarization patterns different from that of 371.6 cm^{-1} , which is associated with Raman tensors of different symmetries [19].

The elemental composition and chemical bonding information of the nanoribbons were acquired by XPS. In Fig. 2(b), the Ti $2p$ peaks at 456 and 462 eV were ascribed to Ti^{4+} bonded with S atoms, whereas the satellite peaks at 458 and 465 eV with a weight of less than 10% were assigned to Ti-O bonds [14]. In the S $2p$ XPS spectrum [Fig. 2(c)], peaks that correspond to S_2^{2-} and S^{2-} were identified, consistent with the sulfur valence states in TiS_3 [20]. The multiplex composition and position of both Ti and S XPS signals agree

well with that observed in pristine bulk TiS_3 [20], and the Ti/S atomic ratio was revealed to be 0.31, in accordance with the theoretical value of TiS_3 (0.33). We note that the slight sulfur excess should be due to elemental sulfur-induced fitting errors (Fig. S5 in the SM). Figure 2(d) is the transmission electron microscope (TEM) image of a TiS_3 nanoribbon along with the corresponding electron diffraction pattern. The edge of the ribbon was found to be parallel to the indexed [010] direction, that is, along the h axis. Further high-angle annular dark-field (HAADF) image taken by scanning TEM (STEM) directly visualized the rectangular atomic structures [Fig. 2(e)], from which the (100) and (010) interplanar distances were measured to be 0.497 and 0.346 nm, respectively, both close to those of bulk TiS_3 (JCPDS 15-0783). Overall, these results demonstrate unambiguously that the synthesized nanosheets and nanoribbons are TiS_3 , a reported n -type semiconductor [21,22].

In contrast to previous reports on mechanically exfoliated TiS_3 that behaves as an n -type semiconductor [8,11], our electrical measurements showed that the CVD-synthesized TiS_3 is highly conductive in both the nanoribbon [Fig. 3(a)] and nanosheet forms (Fig. S6 of the SM). Ohmic contact was evidently achieved for all the devices in Fig. 3(a), showing linear current dependence on the applied voltage even at low temperatures [Fig. 3(c)]. Using the transfer length method, we extracted the contact resistance of $27.5 \text{ k}\Omega \mu\text{m}$, the TiS_3 resistivity of $0.28 \text{ k}\Omega \mu\text{m}$ ($0.028 \Omega \text{ cm}$), and the sheet resistance of $7.84 \text{ k}\Omega/\text{sq}$ for the device [Fig. 3(b)]. The derived conductivity, despite surpassing other low-dimensional semiconductors, is to some extent lower than that of metallic TMTCs such as TaSe_3 [3,5] and ZrTe_3 [4]. The $\text{TiS}_3/\text{TaSe}_3$ conductivity ratio ($\sim 10^{-2}$) is similar to that of degenerately

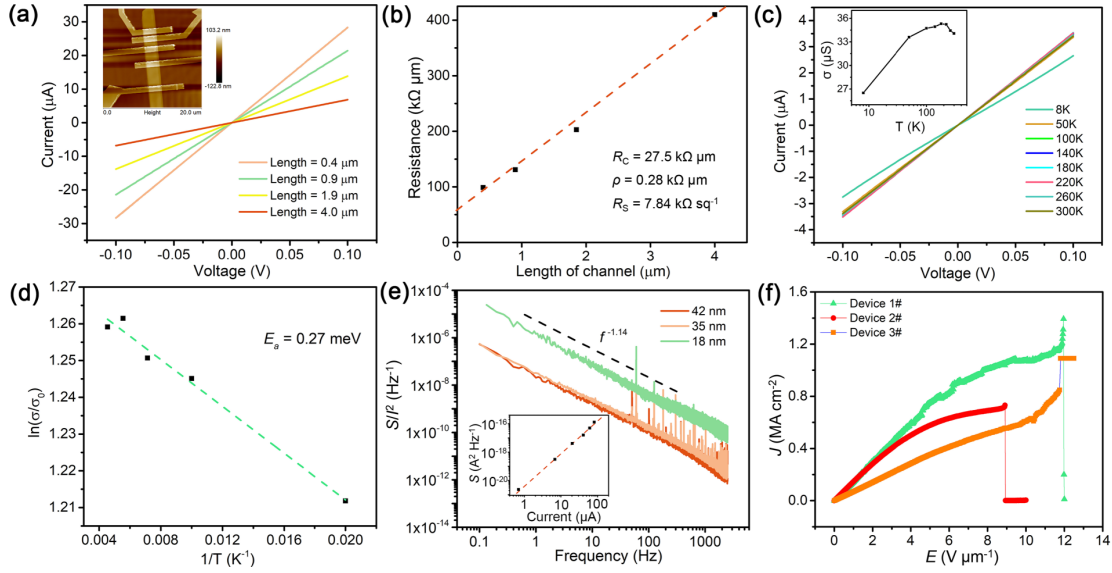


FIG. 3. Electrical measurements of the CVD-synthesized TiS_3 nanostructures. (a) Current-voltage curves of the TiS_3 device with channel lengths varying from 0.4 to 4 μm . The inset shows the AFM image of the device. The channel width and height measured by AFM are 2.5 μm and 35.7 nm, respectively. (b) Plot of the total resistance as a function of the channel length for the device in (a). (c) Current-voltage curves of a 4 $\mu\text{m} \times 2.5 \mu\text{m} \times 35.7\text{-nm}$ TiS_3 device under different temperatures. The inset shows the conductance change with the temperatures. (d) Arrhenius plot of the device in (c). (e) Normalized noise spectral density, S/I^2 , as a function of frequency f for TiS_3 devices with different thicknesses. Voltage = 0.1 V. The inset shows the proportionality of S with the current at $f = 10$ Hz. (f) Current response of a 1 $\mu\text{m} \times 0.31 \mu\text{m} \times 15.6\text{-nm}$ device 1#, 0.9 $\mu\text{m} \times 2.5 \mu\text{m} \times 35.7\text{-nm}$ device 2#, and 0.4 $\mu\text{m} \times 2.5 \mu\text{m} \times 35.7\text{-nm}$ device 3# to the electrical field.

doped semiconductors (such as silicon) versus conventional metals (such as copper) that associates with the carrier density discrepancy of the latter two.

Notably, the high conductivity of the CVD- TiS_3 could be barely modulated by the gate voltage (Fig. S7 of the SM), from which an electron carrier type could be determined with an estimated charge density of $1.12 \times 10^{19} \text{ cm}^{-3}$ (see the SM for more details), typical for that of a degenerately doped semiconductor. With decreasing temperature, the device conductance (σ) increases first, maximizes at ~ 180 K, and then decreases [inset of Fig. 3(c)]. The positive $d\sigma/dT$ in the low-temperature range indicates a thermally activated process that can be fitted with Arrhenius equation [Fig. 3(d)], from which an activation energy of $E_a = 0.27$ meV is derived. Note that this activation barrier takes into account the contribution from both the contacts (contact barrier) and the channel (hopping barrier), and the remarkably small E_a value, combined with the moderate carrier density as compared to that of a metal, suggests that the high conductivity of CVD- TiS_3 is attributed to a heavy doping effect that associates with ionizable defects, according to the impurity conduction model [23,24].

To estimate the quality and reliability of the material as a nanoscale conductor, time-domain current measurements were performed in vacuum, together with the Fourier-transformed current power spectral density (S) being obtained. As a premise for this study, the S proportionality to I^2 at $f = 10$ Hz was verified in experiment [inset of Fig. 3(e)], which demonstrates that current fluctuations were caused by fluctuations in resistance as opposed to being driven by the

applied current [3,25]. Figure 3(e) is the logarithmic plot of the normalized noise spectral density (S/I^2) as a function of frequency f , for TiS_3 of different thicknesses. In all the cases, the noise spectral density is proportional to $1/f^\gamma$ with $\gamma \approx 1$, indicating absence of electromigration [3,5]. The noise level of 18 nm TiS_3 is larger than that of 42 or 35 nm TiS_3 , which might be due to the increasingly significant role of surface disorders below certain thicknesses [25]. With increasing voltage bias, a maximum current density of $1.4 \times 10^6 \text{ A/cm}^2$ is achieved before electrical breakdown [Fig. 3(f)]. This value is higher than that of conventional materials such as Cu [26] and electrically gated MoS_2 multilayers [27], and comparable to the case of gated TiS_3 nanoribbons [8], enabling possibility for the CVD-synthesized TiS_3 as nanoscale conductors.

Furthermore, the three devices in Fig. 3(f), despite having different dimensions, exhibit similar Joule heating powers per unit area and electrical fields when breakdown occurs (Table S1 of the SM). This suggests that both electromigration and Joule heating-induced chemical degradation [8,28] could be responsible for the electrical breakdown observed here. Notably, the as-synthesized TiS_3 nanoribbons, although having nanoscale thicknesses and widths, are stable in ambient conditions and show very slow degradation without any encapsulation for more than 100 d (Fig. S8 of the SM). This is distinctly different from metallic TMTCs such as TaSe_3 , for which timely h -BN encapsulation is necessary to inhibit chemical degradation and property failure [3,5].

As the electrical conductivity is quite robust (as supported by little gating effect) in the CVD-synthesized TiS_3

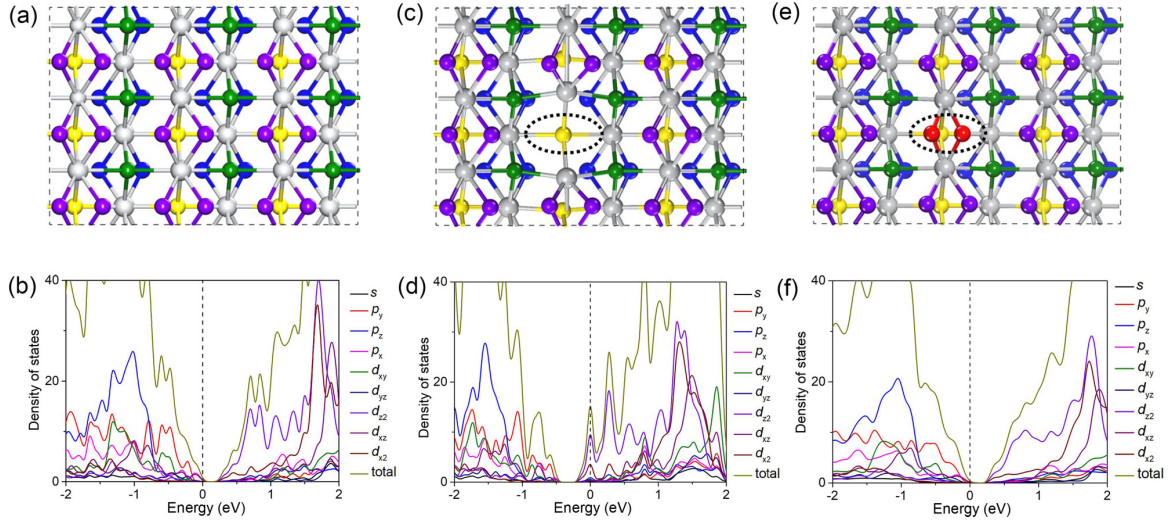


FIG. 4. Theoretical understanding of the vacancy-induced heavy doping in CVD-grown TiS_3 . Shown in the upper row are top-view (3×3) supercells of (a) intrinsic monolayer TiS_3 , (c) monolayer TiS_3 with S_2^{2-} vacancies, and (e) monolayer TiS_3 with the S_2^{2-} vacancies filled by oxygen pairs. For better visualization, S atoms in different layers are presented in different colors. Purple and blue atoms illustrate S_2^{2-} . Yellow and green atoms illustrate S^{2-} . Gray atoms illustrate Ti^{4+} . Red atoms illustrate O_2^{2-} . Dashed circles mark the position of S_2^{2-} vacancies. Corresponding PDOS spectra are presented in (b), (d), and (f), respectively, in the lower row. Dashed lines indicate where the Fermi levels are.

nanostructures regardless of their dimensions, we could tentatively rule out the possibility of extrinsic doping by, for example, interfacial defects. The heavy n -type doping observed here is hence likely to be a contribution of intrinsic defects embedded in the TiS_3 lattice. It has been suggested that sulfur deficiency in TiS_3 is responsible for the doping effect [21]. Here, S_2^{2-} vacancies were deduced to be the major defect type based on the multicomponent fitting result of the S 2p XPS spectrum in Fig. 2(c), showing a $\text{S}_2^{2-}/\text{S}^{2-}$ atomic ratio of ~ 1.53 . This value is distinctly lower than that of pristine TiS_3 [20], which can be formulated as $\text{Ti}^{4+}\text{S}_2^{2-}\text{S}^{2-}$ ($\text{S}_2^{2-}/\text{S}^{2-}$ atomic ratio equals to 2). A recent work by annealing pristine TiS_3 in vacuum also reveals S_2^{2-} vacancies to be the dominant defects in TiS_3 [29].

Our DFT calculations indeed verified that S_2^{2-} vacancies with a finite density could n -type dope TiS_3 up to a degenerate level. To do this, we considered the (3×3) supercells of intrinsic monolayer TiS_3 , monolayer TiS_3 with S_2^{2-} vacancies, and monolayer TiS_3 with the S_2^{2-} vacancies filled by oxygen pairs [Figs. 4(a), 4(c), and 4(e), respectively]. The results are listed in Table S2 of the SM. Monolayer models were employed here for simplicity while providing rational calculation results since TiS_3 band structure is insensitive to thickness [30]. For the pristine case, the TiS_3 lattice after geometric optimization has in-plane periodicities of $a = 4.92 \text{ \AA}$ and $b = 3.44 \text{ \AA}$ [Fig. 4(a)], both in agreement with the TEM results in Fig. 2. The corresponding projected density of states (PDOS) spectrum is shown in Fig. 4(b), exhibiting a band gap of 0.20 eV. It is well documented that DFT with the exchange-correlation functional of the generalized gradient approximation (GGA)–Perdew–Burke–Ernzerhof (PBE) form will underestimate the band gap [31], and our calculated band gap is consistent with previous computational reports [30,32].

When a S_2^{2-} vacancy was introduced into the supercell, the lattice distorted slightly at the defect site [Fig. 4(c)], and a new PDOS peak emerged at the bottom of the conduction band, with the Fermi level residing within it [Fig. 4(d)]. This evidently indicates that S_2^{2-} vacancies serve as n -type dopants for the semiconducting TiS_3 . The spontaneous tendency of generating high-density S_2^{2-} vacancies is supported by their small formation energy of 1.16 eV/atom, which is distinctly lower than that of sulfur vacancies in disulfide materials (1.9–3.2 eV/atom) [33]. Notably, being defective with abundant S_2^{2-} vacancies does not degrade significantly the ampacity of the nanoscale conductor (Fig. 3(f) and Ref. [8]), evidence for the structural stability of the S_2^{2-} vacancies. On the other hand, in order to prevent S_2^{2-} vacancy formation, a synthesis method like CVT would be needed where the sulfur vapor concentration can be much higher than in ambient-pressure CVD conditions.

Last, we ruled out the possibility of electron doping caused by oxygen occupancy in the S_2^{2-} vacancies, which likely occurred at near-surface sites regarding the Ti–O bonding components observed in XPS [Fig. 2(b)]. Our calculations show that the TiS_3 with S_2^{2-} vacancies filled by either oxygen pairs [Figs. 4(e) and 4(f)] or single oxygen atoms (Fig. S9 of the SM) was converted back to a semiconductor with sizable band gaps. Hence the near-surface oxygen substitution should be irrelevant to the heavy doping of TiS_3 , but might be responsible for the current noise associated with surface disorders [Fig. 3(c)]. Interestingly, our calculations also reveal a large diffusion barrier of 2.63 eV for oxygen atoms through the S_2^{2-} vacancy-rich TiS_3 layer (Fig. S10 of the SM). This explains the ambient stability of our CVD- TiS_3 sample despite the inevitable surface oxidation (oxygen filling in the surface S_2^{2-} vacancies).

The above analyses highlight the possibility of continuously tuning the electrical properties of TiS_3 through defect engineering. While S_2^{2-} vacancies are thermodynamically prevalent with less controllable densities, passivating them by oxygen atoms represents an effective way to reduce the carrier densities and recover the semiconducting properties. An *in situ* growth process that incorporates oxygen in the carrier gas could possibly enable the formation of crystalline $\text{TiS}_{3-x}\text{O}_x$ nanostructures, promising as a platform material for quasi-1D electronics.

III. EXPERIMENT

A. Materials

Sulfur powder ($\geq 99.5\%$ purity) and titanium powder (99.98%, trace metal basis) were purchased from Sigma-Aldrich. Ammonium chloride (99.999%, metal basis) was purchased from Alfa Aesar. Mica was purchased from Ted Pella and was mechanically cleaved with fresh surface for the CVD growth.

B. Synthesis of TiS_3

As a pretreatment of dehydration, $\text{Ti}/\text{NH}_4\text{Cl}$ mixture (~ 150 mg, mass ratio of 1:2) was dispersed in acetone and placed for 5 min. After the mixture powder was settled down, the upper supernatant was discarded. This process was repeated twice. Then the mixture was quickly loaded into the CVD system before its drying up.

The TiS_3 nanostructures were grown by CVD using a three-zone furnace with a 1-in.-diameter quartz tube. Commercial sulfur powder, dehydrated $\text{Ti}/\text{NH}_4\text{Cl}$ mixture, and mica substrate were placed from upstream to downstream in separate temperature zones to achieve rigorous control of the precursor evaporation. Before the heating process, 1000 sccm Ar/H_2 (volume ratio of 90:10) was used to purge the reaction tube for 5 min. Under a mixed gas flow of 50 sccm Ar and 10 sccm H_2 , the substrate zone was heated to $370\text{--}450^\circ\text{C}$ within 5 min, after which the sulfur and $\text{Ti}/\text{NH}_4\text{Cl}$ zones were slowly heated to 250 and 225°C , respectively, within 25 min. With a stabilization time of 2 min at these temperatures, the carrier gas flow was switched to 180 sccm Ar and 45 sccm H_2 to effectively transport the generated TiCl_4 precursor for the CVD growth. After 10-min growth, the furnace was cooled down naturally under Ar (100 sccm) and H_2 (50 sccm). Details of the above growth program are illustrated in Fig. S11 of the SM.

C. Characterization

Characterizations were implemented using OM (Axio Imager, Carl Zeiss), Raman (Witec CRM 200 Confocal Raman Microscopy, excitation wavelength of 514 nm), atomic force microscopy (AFM) (Dimension 3100, Veeco Instruments Inc.), XPS (PHI Versaprobe II), scanning electron microscopy (Zeiss Merlin high-resolution SEM), and TEM.

D. Fabrication and measurement of TiS_3 devices

TiS_3 samples were first transferred to 300-nm SiO_2/Si substrate using typical etching transfer or dry transfer mentioned

in the SM. The devices were fabricated by a standard e-beam lithography and metallization processes using 10 nm Ni and 50 nm Au. The electrical performance was studied by using a B1500A Semiconductor Device Analyzer (Agilent Technologies).

E. Computation

Calculations of geometry optimizations and electronic structures are performed based on the DFT in conjunction with the projector-augmented wave pseudopotential [34], as implemented in the Vienna *Ab initio* simulation package (VASP) code [35]. The exchange-correlation functional is treated under the GGA of PBE form [36,37]. van der Waals interaction is taken into account using the semiempirical dispersion correction of DFT-D2 approach [38]. The vacancies were obtained by removing the considered atoms from a 3×3 supercell which consists of 18 Ti atoms and 54 S atoms. A plane-wave cutoff energy of 500 eV is used for the plane-wave expansion of the wave function. Centered grids of $1\times 1\times 1$ and $7\times 7\times 1$ k -points meshes were used to sample the Brillouin zone [39] in the structural optimization and calculate the electronic properties, respectively. To obtain reliable optimized structures, the maximum force was less than 10^{-2} eV/Å per atom and the energies were converged to within 10^{-5} eV between two successive steps. In all cases, lattice parameters were optimized along the x , y , and z directions. In order to screen the interlayer interaction, a vacuum spacing of 15 Å between adjacent layers was chosen.

IV. CONCLUSION

In summary, we explored the CVD synthesis of TiS_3 , an anticipated n -type semiconductor, with controlled morphologies ranging from rectangular nanosheets to quasi-1D nanoribbons. The obtained nanostructures, being well characterized to be the anisotropic TiS_3 lattices, surprisingly exhibit remarkable conductivities, which revealed by experiments and theoretical calculations was due to the high-density S_2^{2-} vacancies in the CVD-grown samples acting as electron dopants. It is postulated that such trichalcogenide semiconductors could enable new possibilities for quasi-1D electronic device paradigms, if they are suitably defect engineered with S_2^{2-} vacancies and oxygen substituents.

ACKNOWLEDGMENTS

The work is supported by National Natural Science Foundation of China (Grants No. 52072204 and No. 51672154) and the National Key R&D Program of China (Grant No. 2016YFA0200200). Q.J. and J.K. acknowledge financial support by the STC Center for Integrated Quantum Materials, NSF Grant No. DMR-1231319. Y.L., J.K., and T.P. acknowledge the U. S. Army Research Office through the Institute for Soldier Nanotechnologies at MIT, under Cooperative Agreement No. W911NF-18-2-0048. C.S., J.W., and J.K. acknowledge the support from the U.S. Army Research Office (ARO) under Grant No. W911NF-18-1-0431. C.S. is currently supported by the Kavli Energy NanoScience Institute/Heising-Simons Fellowship, Berkeley, CA.

M.S. and J.L. contributed equally to this work.

- [1] D. W. Bullett, *J. Phys. C: Solid State Phys.* **12**, 277 (1979).
- [2] J. O. Island, A. J. Molina-Mendoza, M. Barawi, R. Biele, E. Flores, J. M. Clamagirand, J. R. Ares, C. Sánchez, H. S. J. van der Zant, R. D'Agosta, I. J. Ferrer, and A. Castellanos-Gomez, *2D Mater.* **4**, 022003 (2017).
- [3] G. Liu, S. Rumyantsev, M. A. Bloodgood, T. T. Salguero, M. Shur, and A. A. Balandin, *Nano Lett.* **17**, 377 (2017).
- [4] A. Geremew, M. A. Bloodgood, E. Aytan, B. W. K. Woo, S. R. Corber, G. Liu, K. Bozhilov, T. T. Salguero, S. Rumyantsev, M. P. Rao, and A. A. Balandin, *IEEE Electron Device Lett.* **39**, 735 (2018).
- [5] T. A. Empante, A. Martinez, M. Wurch, Y. Zhu, A. K. Geremew, K. Yamaguchi, M. Isarraraz, S. Rumyantsev, E. J. Reed, A. A. Balandin, and L. Bartels, *Nano Lett.* **19**, 4355 (2019).
- [6] J. Dai and X. C. Zeng, *Angew. Chem. Int. Ed.* **54**, 7572 (2015).
- [7] S. Liu, W. Xiao, M. Zhong, L. Pan, X. Wang, H.-X. Deng, J. Liu, J. Li, and Z. Wei, *Nanotechnology* **29**, 184002 (2018).
- [8] A. J. Molina-Mendoza, J. O. Island, W. S. Paz, J. M. Clamagirand, J. R. Ares, E. Flores, F. Leardini, C. Sánchez, N. Agraït, G. Rubio-Bollinger, H. S. J. van der Zant, I. J. Ferrer, J. J. Palacios, and A. Castellanos-Gomez, *Adv. Funct. Mater.* **27**, 1605647 (2017).
- [9] F. Lévy and H. Berger, *J. Cryst. Growth* **61**, 61 (1983).
- [10] A. Lipatov, M. J. Loes, H. Lu, J. Dai, P. Patoka, N. S. Vorobeva, D. S. Muratov, G. Ulrich, B. Kästner, A. Hoehl, G. Ulm, X. C. Zeng, E. Rühl, A. Gruverman, P. A. Dowben, and A. Sinitskii, *ACS Nano* **12**, 12713 (2018).
- [11] M. Randle, A. Lipatov, A. Kumar, C.-P. Kwan, J. Nathawat, B. Barut, S. Yin, K. He, N. Arabchigavkani, R. Dixit, T. Komesu, J. Avila, M. C. Asensio, P. A. Dowben, A. Sinitskii, U. Singiseti, and J. P. Bird, *ACS Nano* **13**, 803 (2019).
- [12] X. Li, W. Cai, J. An, S. Kim, J. Nah, D. Yang, R. Piner, A. Velamakanni, I. Jung, E. Tutuc, S. K. Banerjee, L. Colombo, and R. S. Ruoff, *Science* **324**, 1312 (2009).
- [13] Y.-H. Lee, X.-Q. Zhang, W. Zhang, M.-T. Chang, C.-T. Lin, K.-D. Chang, Y.-C. Yu, J. T.-W. Wang, C.-S. Chang, L.-J. Li, and T.-W. Lin, *Adv. Mater.* **24**, 2320 (2012).
- [14] Z. Gao, Q. Ji, P.-C. Shen, Y. Han, W. S. Leong, N. Mao, L. Zhou, C. Su, J. Niu, X. Ji, M. M. Goulamaly, D. A. Muller, Y. Li, and J. Kong, *ACS Appl. Mater. Interfaces* **10**, 34401 (2018).
- [15] J. L. Murray, *Bull. Alloy Phase Diagr.* **7**, 156 (1986).
- [16] See Supplemental Material at <http://link.aps.org/supplemental/10.1103/PhysRevMaterials.5.094002> for more experimental details and characterization results.
- [17] M. Talib, R. Tabassum, S. S. Islam, and P. Mishra, *RSC Adv.* **9**, 645 (2019).
- [18] J. O. Island, R. Biele, M. Barawi, J. M. Clamagirand, J. R. Ares, C. Sánchez, H. S. J. van der Zant, I. J. Ferrer, R. D'Agosta, and A. Castellanos-Gomez, *Sci. Rep.* **6**, 22214 (2016).
- [19] K. Wu, E. Torun, H. Sahin, B. Chen, X. Fan, A. Pant, D. Parsons Wright, T. Aoki, F. M. Peeters, E. Soignard, and S. Tongay, *Nat. Commun.* **7**, 12952 (2016).
- [20] M. E. Fleet, S. L. Harmer, X. Liu, and H. W. Nesbitt, *Surf. Sci.* **584**, 133 (2005).
- [21] J. O. Island, M. Barawi, R. Biele, A. Almazán, J. M. Clamagirand, J. R. Ares, C. Sánchez, H. S. J. van der Zant, J. V. Álvarez, R. D'Agosta, I. J. Ferrer, and A. Castellanos-Gomez, *Adv. Mater.* **27**, 2595 (2015).
- [22] A. Lipatov, P. M. Wilson, M. Shekhirev, J. D. Teeter, R. Netusil, and A. Sinitskii, *Nanoscale* **7**, 12291 (2015).
- [23] N. F. Mott and W. D. Twose, *Adv. Phys.* **10**, 107 (1961).
- [24] H. Gao, J. Suh, M. C. Cao, A. Y. Joe, F. Mujid, K.-H. Lee, S. Xie, P. Poddar, J.-U. Lee, K. Kang, P. Kim, D. A. Muller, and J. Park, *Nano Lett.* **20**, 4095 (2020).
- [25] G. Liu, S. Rumyantsev, M. S. Shur, and A. A. Balandin, *Appl. Phys. Lett.* **102**, 093111 (2013).
- [26] M. E. Toimil Molares, E. M. Höhberger, Ch. Schaefflein, R. H. Blick, R. Neumann, and C. Trautmann, *Appl. Phys. Lett.* **82**, 2139 (2003).
- [27] R. Yang, Z. Wang, and P. X.-L. Feng, *Nanoscale* **6**, 12383 (2014).
- [28] R. Murali, Y. Yang, K. Brenner, T. Beck, and J. D. Meindl, *Appl. Phys. Lett.* **94**, 243114 (2009).
- [29] Z. Tian, X. Guo, D. Wang, D. Sun, S. Zhang, K. Bu, W. Zhao, and F. Huang, *Adv. Funct. Mater.* **30**, 2001286 (2020).
- [30] J. Kang and L.-W. Wang, *Phys. Chem. Chem. Phys.* **18**, 14805 (2016).
- [31] J. P. Perdew and M. Levy, *Phys. Rev. Lett.* **51**, 1884 (1983).
- [32] F. Iyikanat, H. Sahin, R. T. Senger, and F. M. Peeters, *J. Phys. Chem. C* **119**, 10709 (2015).
- [33] M. H. Naik and M. Jain, *Phys. Rev. Mater.* **2**, 084002 (2018).
- [34] P. E. Blöchl, *Phys. Rev. B* **50**, 17953 (1994).
- [35] G. Kresse and J. Furthmüller, *Phys. Rev. B* **54**, 11169 (1996).
- [36] J. P. Perdew and W. Yue, *Phys. Rev. B* **33**, 8800(R) (1986).
- [37] J. P. Perdew, J. A. Chevary, S. H. Vosko, K. A. Jackson, M. R. Pederson, D. J. Singh, and C. Fiolhais, *Phys. Rev. B* **46**, 6671 (1992).
- [38] S. Grimme, *J. Comput. Chem.* **27**, 1787 (2006).
- [39] H. J. Monkhorst and J. D. Pack, *Phys. Rev. B* **13**, 5188 (1976).